Granular hydrodynamics and pattern formation in vertically oscillated granular disk layers

JOSÉ A. CARRILLO[1], THORSTEN PÖSCHEL[2] AND CLARA SALUEÑA[3]

[1]ICREA (Institució Catalana de Recerca i Estudis Avançats) and Departament de Matemàtiques, Universitat Autònoma de Barcelona, E-08193 Bellaterra, Spain

[2]Charité, Augustenburger Platz 1, 10439 Berlin, Germany

[3]Departament de Enginyeria Mecànica-ETSEQ, Universitat Rovira i Virgili, E-43007 Tarragona, Spain

The goal of this study is to demonstrate numerically that certain hydrodynamic systems, derived from inelastic kinetic theory, give fairly good descriptions of rapid granular flows even if they are way beyond their supposed validity limits. A numerical hydrodynamic solver is presented for a vibrated granular bed in two dimensions. It is based on a highly accurate shock capturing state-of-the-art numerical scheme applied to a compressible Navier–Stokes system for granular flow. The hydrodynamic simulation of granular flows is challenging, particularly in systems where dilute and dense regions occur at the same time and interact with each other. As a benchmark experiment, we investigate the formation of Faraday waves in a two-dimensional thin layer exposed to vertical vibration in the presence of gravity. The results of the hydrodynamic simulations are compared with those of event-driven molecular dynamics and the overall quantitative agreement is good at the level of the formation and structure of periodic patterns. The accurate numerical scheme for the hydrodynamic description improves the reproduction of the primary onset of patterns compared to previous literature. To our knowledge, these are the first hydrodynamic results for Faraday waves in two-dimensional granular beds that accurately predict the wavelengths of the two-dimensional standing waves as a function of the perturbation's amplitude. Movies are available with the online version of the paper.

1. Introduction

Interest has been growing in the hydrodynamic simulation of complex granular flows, with the aim of understanding the details of transport in the continuum limit (Goldhirsch 2003). Because they are both highly nonlinear and non-local, the mechanisms of granular transport in the dense limit are still obscure. The microscopic basis of the hydrodynamic approaches to granular flow is the standard kinetic theory for molecular gases, except for the fact that it includes dissipation (via a constant or velocity dependent restitution) on collision. While strictly speaking hydrodynamic descriptions cease to be valid near the close-packing limit and at low coefficients of normal restitution, such models have been used successfully in situations that are a long way from their supposed limits of validity, to describe, for instance, shock waves in granular gases (Bougie *et al.* 2002; Rericha *et al.* 2002), clustering (Hill & Mazenko 2003; Brilliantov *et al.* 2004) and coexisting phases (Meerson *et al.* 2003, 2004). The difficulty of a hydrodynamic description of granular materials has been addressed in

well-reasoned terms in Goldhirsch (1999, 2001). One cannot pretend to overcome the problems of the hydrodynamic description; however, where it works exceptionally well, one should ask how and why.

In order to compensate for the energy lost in collisions, the typical forcing mechanism, which is periodic vibration, induces not only various interesting phenomena but also the propagation of shock waves originating from the moving boundary into the system. The flow developed under these conditions is supersonic and consequently, steep gradients arise in the hydrodynamic fields. For careful hydrodynamic simulations, it is therefore desirable to use shock-capturing methods to track the sharp fronts, as well as high-order schemes to provide an accurate definition of the profiles. To our knowledge, only direct finite-difference methods have been applied in the literature to solve the Navier–Stokes equations for granular media. These methods do not yield the correct speed of wave propagations since they do not use numerical flux decomposition in local variables. Moreover, most of these methods are inappropriate owing to the implicit or artificial diffusion added to handle supersonic flow.

In order to show the potential of state-of-the-art hydrodynamic simulations (HD) applied to granular matter, in this paper we address a paradigmatic problem of granular dynamics: the observation of Faraday waves and the quantitative description/comparison of the instability via both hydrodynamic simulations based on weighted essentially non-oscillatory (WENO) schemes and the well-established method of event-driven molecular dynamics (MD). A hydrodynamic code has two difficulties in solving this kind of systems: first, proper parameters must be used and the code must be finely tuned in order to reproduce the instability of the flat state which induces periodic patterns. Secondly, the numerical scheme must capture the propagation of shock waves across the granular bed under vibration and the discontinuities involved.

The onset of patterns in vertically oscillated granular layers has been numerically investigated via particle and hydrodynamic simulations by Bougie *et al.* (2005). The numerical scheme employed there to solve the granular Navier–Stokes equations is based upon finite differences plus artificial diffusion. They make a thorough analysis of the role of fluctuations in pattern inception and the dependence of pattern inception on the acceleration parameter, and the results mainly refer to the mean square displacement of the local centre of mass of the granular layer as an order parameter. Our analysis, on the other hand, is concerned with the instability of the flat state and how periodic patterns are reproduced. By comparing particle and hydrodynamic simulations, we assess the validity of granular hydrodynamic simulations in complex flow problems.

The paper is organized as follows: in § 2, we summarize the hydrodynamic description of rapid granular flows based on kinetic theory. Section 3 explains the details of the hydrodynamic code. In § 4, we describe the numerical hydrodynamic experiment and the molecular dynamics experiment, the results of which are analysed and compared in § 5. In the conclusions, we summarize our findings and make a final comparison of both methods.

2. Granular kinetic theory and hydrodynamics

As usual in granular kinetic theory, we follow the evolution of the number density of particles in phase space (Brilliantov & Pöschel 2004). Given a two-dimensional granular gas composed of homogeneous disks of diameter $\sigma > 0$ and given (x, V_1),

$(x - \sigma n, V_2)$ the states of two particles, pairs of their position and velocity, before the collision, where $n \in S^1$ is the unit vector along the disk centres, the postcollisional velocities are found by assuming that a fraction of the normal relative velocity is lost while its orthogonal component is unchanged. As a consequence, the postcollisional velocities are obtained as

$$V_1' = \tfrac{1}{2}(V_1 + V_2) + \tfrac{1}{2}V', \tag{2.1a}$$

$$V_2' = \tfrac{1}{2}(V_1 + V_2) - \tfrac{1}{2}V', \tag{2.1b}$$

where $V' = V - (1 + e)(V \cdot n)n$, $V = V_1 - V_2$ and $V' = V_1' - V_2'$, with e being the *constant* coefficient of restitution. Let us denote by V_1^* and V_2^* the precollisional velocities corresponding to V_1 and V_2. The Boltzmann–Enskog equation for inelastic hard disks gives the evolution of $f(t, x, V_1)$ and it can be written as

$$\frac{\partial f}{\partial t} + (V_1 \cdot \nabla_x)f = \sigma^2 Q(f, f), \tag{2.2}$$

where the collision operator is given by

$$Q(f, f)(t, x, V_1) = g_o(\nu) \int_{\mathbb{R}^2} \int_{S_+^1} [(V_1 - V_2) \cdot n] \left[\frac{1}{e} J f(t, x, V_1^*) f(t, x - \sigma n, V_2^*) \right.$$
$$\left. - f(t, x, V_1) f(t, x + \sigma n, V_2) \right] dn \, dV_2,$$

in which dense gas effects are taken into account through the pair correlation function $g_o(\nu)$, where ν is the two-dimensional volume fraction: i.e. $\nu = \pi \rho \sigma^2 / 4$. The notation S_+^1 means that the above integral on n is computed over those values of n such that $((V_1 - V_2) \cdot n) > 0$. Factor J is the Jacobian of the transformation between post- and precollisional velocities, where $J = 1/e$ in the constant restitution coefficient case. The moments of f allow us to compute the macroscopic quantities: the number density

$$\rho(t, x) = \int_{\mathbb{R}^2} f(t, x, V_1) \, dV_1, \tag{2.3}$$

the velocity field

$$U(t, x) = \frac{1}{\rho} \int_{\mathbb{R}^2} V_1 f(t, x, V_1) \, dV_1, \tag{2.4}$$

and the granular temperature

$$T(t, x) = \frac{1}{2\rho} \int_{\mathbb{R}^2} |V_1 - U(t, x)|^2 f(t, x, V_1) \, dV_1. \tag{2.5}$$

Several formulae have been proposed for $g_o(\nu)$ in the literature, but we have chosen the convenient formulae obtained by Torquato (1995). More precisely, we use

$$g_o(\nu) = \begin{cases} \dfrac{1 - 0.436\nu}{(1 - \nu)^2} & \text{for } 0 \leqslant \nu < \nu_f, \\[2mm] \dfrac{1 - 0.436\nu_f}{(1 - \nu_f)^2} \dfrac{\nu_c - \nu_f}{\nu_c - \nu} & \text{for } \nu_f \leqslant \nu \leqslant \nu_c, \end{cases} \tag{2.6}$$

where $\nu_f = 0.69$ and $\nu_c = 0.82$ are the freezing packing fraction and the random close packing fraction, respectively. Their values are taken from the reference above. The reason for using this formula is that in our analysis we want to go past the freezing point and approach the critical packing fraction with reasonable accuracy.

The value of the close random packing fraction $\nu_c = 0.82$, instead of the hexagonal packing fraction $\nu_c = 0.92$ can be justified *a posteriori*, when comparing the results of MD and HD simulations.

Expansion methods (Jenkins & Richman 1985*a*; Goldshtein & Shapiro 1995) were used to obtain hydrodynamic equations for the two-dimensional granular gas,

$$\frac{\partial \rho}{\partial t} + \nabla \cdot (\rho \boldsymbol{U}) = 0, \tag{2.7a}$$

$$\rho \left(\frac{\partial \boldsymbol{U}}{\partial t} + (\boldsymbol{U} \cdot \nabla)\boldsymbol{U} \right) = \nabla \cdot \boldsymbol{P} + \rho \boldsymbol{F}, \tag{2.7b}$$

$$\rho \left(\frac{\partial T}{\partial t} + (\boldsymbol{U} \cdot \nabla)T \right) = -\nabla \cdot \boldsymbol{q} + \boldsymbol{P} : \boldsymbol{E} - \gamma. \tag{2.7c}$$

They represent the evolution of the number density of particles $\rho(t, \boldsymbol{x})$, the velocity field $\boldsymbol{U}(t, \boldsymbol{x}) = (U_1, U_2)(t, \boldsymbol{x})$ and the granular temperature $T(t, \boldsymbol{x})$. The tensor $\boldsymbol{P} = (P_{ij})$ is the pressure tensor, given in terms of the tensor $\boldsymbol{E} = (E_{ij})$ by

$$P_{ij} = \left[-p + (2\mu_1 - \mu_2) \sum_i E_{ii} \right] \delta_{ij} + 2\mu_2 E_{ij}, \tag{2.8}$$

with

$$E_{ij} = \frac{1}{2} \left(\frac{\partial U_i}{\partial x_j} + \frac{\partial U_j}{\partial x_i} \right). \tag{2.9}$$

The principal pressure is related to the density and the temperature through the equation of state

$$p = \rho \epsilon \left[1 + (1 + e)G(\nu) \right]. \tag{2.10}$$

It includes a correction to the usual perfect gases law, $p = \rho \epsilon$, with the internal energy density $\epsilon = T$ in two dimensions and $G(\nu) = \nu g_o(\nu)$, proposed by Jenkins & Richman (1985*a*); Goldshtein & Shapiro (1995); Brilliantov *et al.* (2004) to incorporate dense gas effects. The vector $\boldsymbol{q} = -\chi \nabla T$ models the heat flux. The viscosities μ_1 and μ_2, the thermal conductivity χ and the cooling coefficient γ are density and temperature dependent whose explicit expression we take from Jenkins & Richman (1985*a,b*). The bulk viscosity is given by

$$\mu_1 = \frac{2}{\sqrt{\pi}} \rho \sigma T^{1/2} G(\nu) \tag{2.11}$$

and the shear viscosity by

$$\mu_2 = \frac{\sqrt{\pi}}{8} \rho \sigma T^{1/2} \left[\frac{1}{G(\nu)} + 2 + \left(1 + \frac{8}{\pi} \right) G(\nu) \right], \tag{2.12}$$

the thermal conductivity is

$$\chi = \frac{\sqrt{\pi}}{2} \rho \sigma T^{1/2} \left[\frac{1}{G(\nu)} + 3 + \left(\frac{9}{4} + \frac{4}{\pi} \right) G(\nu) \right] \tag{2.13}$$

and the cooling coefficient is

$$\gamma = \frac{4}{\sigma \sqrt{\pi}} \left(1 - e^2 \right) \rho T^{3/2} G(\nu). \tag{2.14}$$

More involved hydrodynamic models incorporate higher-order terms in the gradients expansion (Goldhirsch 2003), and more accurate expressions for the kinetic coefficients which include extra terms for moderately dense gases and/or finite inelasticity

corrections (Garzó & Dufty 1999; Lutsko 2005; Serero *et al.* 2007). In principle, any kind of constitutive relations can be easily implemented. The major drawback is that there is a lack of accurate constitutive relations for two-dimensional granular systems with density corrections and/or finite degree of inelasticity. This is why we stick to the inaccurate although widely used Jenkins & Richman (1985a,b) expressions. Finally, the vector field F represents the external force acting on the system: for instance, gravity modulated by the piston movement changing to the moving piston reference frame. The mathematical validity of the hydrodynamic approximation in the Euler case was discussed in Bobylev, Carrillo & Gamba (2000).

3. Details of the hydrodynamic code

In order to simulate the granular Navier–Stokes equations (2.7) numerically, we write them as corrections to a compressible Euler-type system in conservation form. In fact, we consider the equivalent system

$$\frac{\partial \rho}{\partial t} + \nabla \cdot (\rho U) = 0, \tag{3.1a}$$

$$\frac{\partial (\rho U)}{\partial t} + \nabla \cdot [\rho (U \otimes U)] + \nabla p = \nabla \cdot P + \rho F, \tag{3.1b}$$

$$\frac{\partial W}{\partial t} + \nabla \cdot [UW] = -\nabla \cdot q + P : E + U \cdot (\nabla \cdot P) - \gamma + \rho(U \cdot F), \tag{3.1c}$$

where the total energy density W is given by

$$W = \rho T + \tfrac{1}{2}\rho |U|^2 = \rho \epsilon + \tfrac{1}{2}\rho |U|^2. \tag{3.2}$$

The system (3.1) can be rewritten as

$$\frac{\partial u}{\partial t} + \frac{\partial}{\partial x_1} f(u) + \frac{\partial}{\partial x_2} g(u) = S(u) \tag{3.3}$$

with $x = (x_1, x_2)$, obvious definitions for $f(u)$, $g(u)$ and $S(u)$ (see Appendix) and with the vector $u = (u_1, u_2, u_3, u_4)$ whose components are given by

$$\left. \begin{aligned} u_1 &= \rho, \quad u_2 = \rho U_1, \quad u_3 = \rho U_2, \\ u_4 &= \rho \epsilon + \tfrac{1}{2}\rho |U|^2 = \rho \epsilon + \tfrac{1}{2}\rho \left(U_1^2 + U_2^2 \right). \end{aligned} \right\} \tag{3.4}$$

As a consequence, equations (3.1) have the structure of a system of nonlinear conservation laws with sources. Local eigenvalues and both local left- and right-eigenvectors of the Jacobian matrices $f'(u)$ and $g'(u)$ are explicitly computable and included in the Appendix. Let us just mention at this point that these quantities depend on the sound speed c_s. For a general equation of state in which the pressure is a general function of density and enthalpy $p = p(\rho, \epsilon)$, the sound speed is given by

$$c_s^2 = \frac{\partial p}{\partial \rho} + \frac{p}{\rho^2} \frac{\partial p}{\partial \epsilon} = p_\rho + \frac{p}{\rho^2} p_\epsilon. \tag{3.5}$$

Therefore, in order for the sound speed to be well defined, the pressure must have first partial derivatives as a function of ρ and ϵ. In the particular case of the chosen equation of state (2.10), p is a function of v and thus of ρ through the function $G(v)$, then $G(v)$ is smoothed out around the freezing point volume fraction v_f in order to make it C^1 by a simple Hermite interpolation in a tiny interval around v_f. We remark that the system (3.1) has been solved in dimensional variables for convenience of comparison to molecular dynamics simulations.

The numerical method applies a high-order shock-capturing scheme for the convective Euler part of this system: i.e. the left-hand side of (3.3), while the terms on the right-hand side $S(u)$, forcing and Navier–Stokes terms, are either directly evaluated or approximated by second-order central finite differences.

The convective terms $(\partial/\partial x_1)f(u)$ and $(\partial/\partial x_2)g(u)$ are approximated by a fifth-order finite-difference characteristic-wise WENO method in a uniform grid following Jiang & Shu (1996). This scheme is a well-known shock-capturing and high-order method for nonlinear conservation laws that has been adapted to our situation. For the sake of self-consistency of the paper, we explain the numerical method in detail below. Extensive benchmarks have shown this method to be particularly well adapted to control oscillations in shock regimes in classical Euler equations for gases (see the survey by Shu 1998).

As will be explained in § 5, the forcing gives rise to shocks in our benchmark experiment. They appear neatly in volume fraction and temperature, as reported in Bougie *et al.* (2005). These shocks are of course regularized by Navier–Stokes terms to large gradient regions, but numerically, they do give the same problems. The salient property of WENO schemes is that they are high-order discretization methods (fifth-order in space for WENO5) which still give accurate approximations near shock regions.

We first restrict ourselves to the one-dimensional procedure and work in a dimension by dimension fashion to reconstruct each of the fluxes in (3.3). This means that when approximating $(\partial/\partial x_1)(f(u))$, for example, the other variable x_2 is fixed and the approximation is performed along the x_1 line. Given a uniform grid r_i for any of the spatial variables denoted by r, let us call $u_i(t)$ the numerical approximation to the point value $u(r_i, t)$. The corresponding convective term is approximated as

$$\frac{\partial}{\partial r}f(u) \simeq \frac{\hat{f}_{i+1/2} - \hat{f}_{i-1/2}}{\Delta r} \tag{3.6}$$

where $\hat{f}_{i+1/2}$ is the numerical flux.

Let us briefly describe the general characteristic-wise finite-difference procedure with flux splitting and flux reconstruction. At each fixed time t, we find the numerical fluxes $\hat{f}_{i+1/2}$ in the following way:

Step 1. We first compute an average or intermediate state $u_{i+1/2}$ using Roe's formula as in Shu (1998) and Kamenetsky *et al.* (2000).

Step 2. We compute the matrices of right R and left R^{-1} eigenvectors and eigenvalues $\Lambda_l(u_{i+1/2})$, $l = 1, \ldots, 4$, of the Jacobian matrix $f'(u_{i+1/2})$ from the formulae in the Appendix to obtain

$$
\begin{aligned}
R &= R(u_{i+1/2}) \quad R^{-1} = R^{-1}(u_{i+1/2}), \\
\Lambda &= \Lambda(u_{i+1/2}) = \text{diag}[\Lambda_l(u_{i+1/2})].
\end{aligned}
\tag{3.7}
$$

Step 3. We transform the values u_i and $f(u_i)$ in the potential stencil of the approximation of the flux to the local characteristic coordinates by using the left eigenvectors:

$$v_i = R^{-1}u_i, \quad h_i = R^{-1}f(u_i). \tag{3.8}$$

Step 4. We use global Lax–Friedrichs flux splitting with the transport coefficient computed from the maximum, in absolute value, of the eigenvalues computed above to obtain $h_i^{\pm}$ from

$$h_i^{\pm} = \tfrac{1}{2}(h_i \pm \alpha v_i), \tag{3.9}$$

where the dissipation parameter α is given by

$$\alpha = \max_{i,l} |\Lambda_l(\boldsymbol{u}_{i+1/2})|. \tag{3.10}$$

Step 5. We compute the decomposed fluxes $\hat{\boldsymbol{h}}^+_{i+1/2}$ and $\hat{\boldsymbol{h}}^-_{i+1/2}$ at the middle points using the high-order reconstruction explained below.

Step 6. We transform the computed fluxes back to the physical space by using the right eigenvectors

$$\hat{\boldsymbol{f}}^\pm_{i+1/2} = \boldsymbol{R}\hat{\boldsymbol{h}}^\pm_{i+1/2}, \tag{3.11}$$

and, finally, we add them to obtain the final numerical flux

$$\hat{\boldsymbol{f}}_{i+1/2} = \hat{\boldsymbol{f}}^+_{i+1/2} + \hat{\boldsymbol{f}}^-_{i+1/2}. \tag{3.12}$$

Instead of the Roe mean and Lax–Friedrichs flux splitting formulae, we can use more sophisticated and improved methods to avoid numerical diffusion. However, in this case we do not need them since Navier–Stokes terms will have a regularizing effect on shock waves in the flow.

In the WENO5 method, the fluxes in Step 5 are reconstructed with a nonlinear non-local convex combination of three different approximations of the flux by three different local stencils using the flux upwinding. The contribution of each approximation to the computation of the final flux value depends on the local smoothness of the function measured by smoothness indicators based on the local divided differences. If the function is smooth, the resulting approximation is fifth order. The idea behind this weighted approximation is that those stencils with a discontinuity or high gradient will receive almost zero weight in the approximation and so oscillations will be avoided while keeping a high-order approximation in the smooth parts of the flow.

More precisely, let us denote by $\hat{h}^+_{i+1/2,l}$ the lth component of the local numerical flux $\hat{\boldsymbol{h}}^+_{i+1/2}$ and by $h^+_{i,l}$ the lth component of the local flux $\boldsymbol{h}^+_i$. Since the computations below are analogous component by component and fixed for the chosen upwinding, we have decided not to use the sub- and superindex ^+_l for notational simplicity. We obtain the numerical flux $\hat{h}_{i+1/2}$ by

$$\hat{h}_{i+1/2} = \omega_1 \hat{h}^{(1)}_{i+1/2} + \omega_2 \hat{h}^{(2)}_{i+1/2} + \omega_3 \hat{h}^{(3)}_{i+1/2}, \tag{3.13}$$

where $\hat{h}^{(m)}_{i+1/2}$ are the three third-order fluxes on three different stencils given by

$$\hat{h}^{(1)}_{i+1/2} = \tfrac{1}{3}h_{i-2} - \tfrac{7}{6}h_{i-1} + \tfrac{11}{6}h_i, \tag{3.14a}$$

$$\hat{h}^{(2)}_{i+1/2} = -\tfrac{1}{6}h_{i-1} + \tfrac{5}{6}h_i + \tfrac{1}{3}h_{i+1}, \tag{3.14b}$$

$$\hat{h}^{(3)}_{i+1/2} = \tfrac{1}{3}h_i + \tfrac{5}{6}h_{i+1} - \tfrac{1}{6}h_{i+2}. \tag{3.14c}$$

The nonlinear weights ω_m are given by

$$\omega_m = \frac{\tilde{\omega}_m}{\displaystyle\sum_{l=1}^{3} \tilde{\omega}_l}, \tag{3.15a}$$

$$\tilde{\omega}_l = \frac{\gamma_l}{(\varepsilon + \beta_l)^2}, \tag{3.15b}$$

with the linear weights γ_l given by

$$\gamma_1 = \tfrac{1}{10}, \quad \gamma_2 = \tfrac{3}{5}, \quad \gamma_3 = \tfrac{3}{10}, \tag{3.16}$$

and the smoothness indicators β_l given by

$$\beta_1 = \tfrac{13}{12}(h_{i-2} - 2h_{i-1} + h_i)^2 + \tfrac{1}{4}(h_{i-2} - 4h_{i-1} + 3h_i)^2, \quad (3.17a)$$

$$\beta_2 = \tfrac{13}{12}(h_{i-1} - 2h_i + h_{i+1})^2 + \tfrac{1}{4}(h_{i-1} - h_{i+1})^2, \quad (3.17b)$$

$$\beta_3 = \tfrac{13}{12}(h_i - 2h_{i+1} + h_{i+2})^2 + \tfrac{1}{4}(3h_i - 4h_{i+1} + h_{i+2})^2. \quad (3.17c)$$

Finally, ε is a parameter that prevents the denominator from becoming zero and is taken as $\varepsilon = 10^{-6}$ in the computation of this paper. The computation for approximating $\hat{h}_{i+1/2}^-$ is obtained with the alternate upwinding by mirror symmetry with respect to the index $i + 1/2$. Shu (1998) gives further details about WENO reconstruction procedures, smoothness indicators, benchmarks and references for different applications.

Finally, the resulting ODE system is solved in time by an explicit third-order total variation diminishing Runge–Kutta scheme introduced by Shu & Osher (1998) with a local Courant–Friedrichs–Lewy (CFL) numerical stability condition at every time step, which ensures that the numerical speed is not less than the largest eigenvalue of the local Jacobian matrix. This is definitely an advantage of WENO methods over many others in computational fluid dynamics (CFD): that is, in order to be numerically stable they must integrate implicitly in time.

The numerical stability CFL condition becomes more restrictive as we approach the random close packing volume fraction. Although viscosity and thermal conductivity NS terms are treated as sources, they are taken into account in the CFL condition since diffusion effectively paces the time stepping of the code. This is due to the dependence of the viscosity and thermal conductivity on the volume fraction, which results in diverging coefficients for both random close packing and vacuum limits. Both limits are avoided in the computation shown in this paper by establishing limits for the volume fraction. These limits are 10^{-4} and 99.99% of the maximum volume fraction. Finally, let us emphasize that the cooling term in the temperature equation in (2.7) is stiff as the particle diameter becomes smaller. In fact, analysing the dimensionless cooling factor, it is not difficult to see that it is of the order of $\eta^{-1/2}G(\nu)$ with the dimensionless parameter $\eta = \sigma\omega^2/g$. Again, the dependence on $G(\nu)$ makes this term stiffer in near-vacuum regions. A similar analysis shows that the viscosity terms have an analogous dependence on these parameters. As the particle diameter becomes smaller, we see a need for an implicit treatment of the NS terms and/or the cooling term in order to avoid very restrictive CFL conditions. Nevertheless, numerical results are quite robust and stable by mesh-refinement even if the CFL condition given by NS terms is not strictly imposed for the reported particle diameter. However, a fully implicit scheme would dramatically increase the computational cost. Implicit–explicit Runge–Kutta schemes (Pareschi & Russo 2005), in which stiff terms are treated implicitly, would be good candidates for computing efficiently at smaller particle diameters.

4. Numerical experiments

4.1. *Structures in vertically oscillated granular systems*

When granular matter is exposed to vertical oscillations in the presence of gravity, spatio-temporal structures are observed at the free surface. Although this was reported as early as 1831 by Faraday, the effect has been systematically studied only recently and a variety of patterns have been observed (e.g. Pak & Behringer 1993; Melo, Umbanhowar & Swinney 1994, 1995; Umbanhowar, Melo & Swinney 1996, 1998;
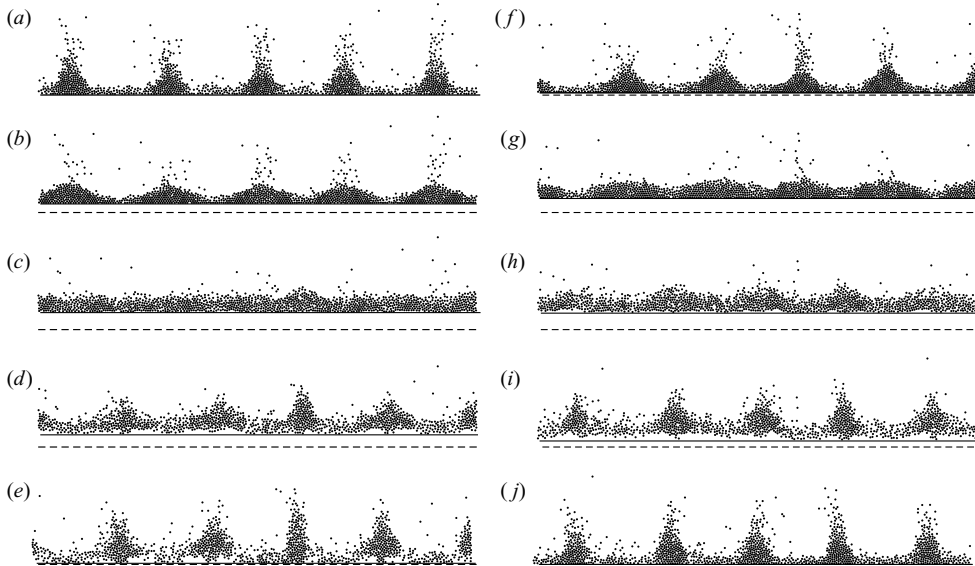
FIGURE 1. Periodic wave-like pattern in a vertically vibrated granular layer. The period of the pattern is twice the period of the excitation. The figure shows a two-dimensional MD simulation of 3000 particles at $A = 4.02$, $f = 3.5$ (for details see below). Only a part of the system is shown. The dashed line indicates the lower amplitude of the oscillation. See movie 1, available with the online version of the paper.

van Doorn & Behringer 1997; Metcalfe, Knight & Jaeger 1997). Theoretical models have been made by Tsimring & Aranson (1997) and Rothman (1998).

Here we focus on subharmonic instabilities in a vertically vibrated layer of granular matter, first reported by Douady, Fauve & Laroche (1989) and then characterized in dependence on the vibration parameters by Clément *et al.* (1996) and Wassgren, Brennen & Hunt (1996). Above a certain amplitude of acceleration, $\Gamma = A\omega^2/g$ (A is the amplitude, ω the angular frequency of the sinusoidal excitation, g is gravity), a periodic wave-like pattern appears with frequency $\omega/2$. Although the condition $\Gamma > 1$ is not necessary for pattern formation (Pöschel, Schwager & Salueña 2000; Renard *et al.* 2001), in all experimental observations the onset of the pattern formation was observed for $\Gamma \gtrsim 4$.

These waves were reproduced in quantitative agreement with numerical MD simulations by Luding *et al.* (1996), Luding (1997*a*) and Aoki & Akiyama (1996) (see also Bizon *et al.* 1997; Aoki & Akiyama 1997) and they were also found from a linear stability analysis of an oscillating granular layer, modelled as an isothermal incompressible fluid with vanishing surface tension (Bizon, Shattuck & Swift 1999). Figure 1 shows snapshots of a molecular dynamics simulation.

We should stress that we are considering frictionless disks, so there is no reason to expect the same curve (wavelength of the pattern versus amplitude) as in experiments. In fact, it has already been reported by Moon, Swift & Swinney (2004) that if friction is neglected, the onset of stripe patterns for three-dimensional-MD simulations is around $\Gamma \simeq 2$, as obtained in our results. The value of the onset of patterns has been discussed by Bougie *et al.* (2005) and found to be between 1.95 and 2.2 for both MD and HD simulations. Here, we want to focus on the comparison between the MD and HD pattern wavelengths as a function of the perturbation amplitudes for the same set of parameters.

It is difficult to make a CFD simulation of such a system since the granular material occurs in the dense state (e.g. figure 1*b*, *c*) and in the dilute state (e.g. figure 1*d*, *e*). A universal CFD computation should be capable of describing the system in both the dense and dilute states.

The described effect and its dependence on the system parameters has been much studied in the literature; in the present paper, it serves as an example to show that our CFD simulation is in quantitative agreement with MD simulations and, thus, capable of describing the time-dependent behaviour of granular systems in the dense and dilute state. For simplicity and better visual representation, here we restrict ourselves to a two-dimensional system. The generalization to three dimensions is conceptually simple although computationally expensive.

4.2. *Set-up of the molecular dynamics system*

Our reference system is an event-driven molecular dynamics simulation (see figure 1). In event-driven MD, each of the N particles in the system moves along a parabolic trajectory due to gravity g. This motion is interrupted by binary collisions, where each of the collision partners changes its velocity according to (2.1). Given particle positions and velocity at time t, the time of the next collision in the entire system can be computed analytically. Therefore, in event-driven simulations, time progresses in irregular steps, from event to event; i.e. from one collision to the next. Unlike force-based MD, in which Newton's equation of motion is solved numerically by evaluating the interaction forces, event-driven MD does not solve Newton's equation explicitly. Instead, Newton's equation is implied in the coefficient of restitution which relates the relative particle velocity after a collision to the velocity before the collision, (2.1); that is, the coefficient of restitution itself which, in general, is a function of material parameters and impact velocity is a result of solving Newton's equation (Brilliantov *et al.* 1996; Schwager & Pöschel 1998; Ramírez *et al.* 1999). In the present paper, we assume that the coefficient of restitution is a material constant and that it adopts the value $e = 0.75$.

The main precondition for applying event-driven MD is the assumption of binary collisions. This implies hard particles. Although conceptually simple, an efficient implementation of event-driven MD algorithms is far more complex than force-based algorithms (see, e.g. Pöschel & Schwager 2005). To compare particle dynamics with hydrodynamics, event-driven MD must be used since both MD and HD simulations are based on the same equations, (2.1), which use both the concept of binary collisions and the coefficient of restitution. In general, there is no simple correspondence between force-based MD and hydrodynamics.

The disadvantage of event-driven MD is that it is restricted to binary and thus, instantaneous collisions. While for dilute granular gases this assumption is justified, for systems with gravity, mathematical reasons prevent us from excluding tree–particle interactions (also called *inelastic collapse*, McNamara & Young 1993). The appearance of the collapse is one serious hint, out of several others, that the hard-sphere model is limited to the dilute case. There are several numerical tricks for preventing or delaying the inelastic collapse in MD simulations, provided the density is low enough. Here we apply the TC-method introduced by Luding & McNamara (1998): if a particle experiences two collisions separated by a lapse of time less than t_c, a multi-particle event is assumed to occur, and the second collision dissipates no energy. In this way, the infinite sequence of collisions is interrupted. For a detailed description and theoretical foundation see Luding & McNamara (1998). In our simulations we used $t_c = 10^{-8}$. Less than the fraction 10^{-6} of all collisions needed to be corrected in this way.

Γ	N	f	A	L	H	N_p	λ	$d\lambda$	L/N_p
2.00	1879	5.5	1.64	300	6	15	18	21	20.00
2.00	2506	5.0	1.99	400	6	16	25	18	25.00
2.00	2506	4.5	2.45	400	6	13	31	18	30.76
2.00	2506	4.0	3.12	400	6	11	37	15	36.36
2.00	3132	3.5	4.02	500	6	12	42	5	41.66
2.00	3759	3.0	5.50	600	6	12	50	10	50.00
2.25	1566	6.0	1.55	250	6	12	21	9	20.83
2.25	1879	5.5	1.85	300	6	13	23	7	23.07
2.25	2506	5.0	2.24	400	6	15	27	4.5	26.66
2.25	2506	4.5	2.76	400	6	14	29	4.5	28.57
2.25	3759	4.0	3.51	600	6	19	31	2	31.57
2.25	3759	3.5	4.52	600	6	14	43	7	42.85
2.25	3759	3.0	6.19	600	6	12	50	13	50.00
2.52	1880	5.5	2.07	300	6	15	20	9	20.00
2.52	1880	5.0	2.50	300	6	12	25	7	25.00
2.52	1880	4.5	3.09	300	6	11	27	6	27.27
2.52	1880	4.0	3.90	300	6	9	33	6	33.33
2.52	3132	3.5	5.07	500	6	12	42	7	41.66
2.52	3132	3.0	6.92	500	6	10	50	16	50.00
2.75	3132	3.5	5.57	500	6	13	39	8	38.46
2.75	3132	3.0	7.59	500	6	9	56	13	55.55
2.75	3759	2.5	10.9	600	6	9	67	15	66.66

TABLE 1. Performed MD simulations. N, number of particles; $f = \omega/2\pi$, frequency of the oscillating bottom wall (in Hz); A, amplitude of the oscillation; L, system width; H, number of particle layers. The observed patterns are characterized by N_p, number of peaks; λ, wave length; $d\lambda$, standard deviation of the measured wavelength over 50 cycles. All lengths are given in units of the particle diameter.

To compare event-driven simulations with CFD results, we performed simulations of an assembly of N particles of diameter $\sigma = 10$ mm, colliding according to (2.1) with a coefficient of restitution $e = 0.75$. The width of the system is L. After the transient time and once the pattern was almost periodic with period $2/f$, where f is the frequency, we recorded the horizontal positions of all particles for 50 periods. The number of peaks N_p of this pattern was then determined by visually inspecting the histogram of this data. In addition, we also determined the wavelengths λ of the pattern by Fourier analysis, which is in good agreement with the values for N_p.

Table 1 shows the parameters of the event-driven MD simulations performed and the results for N_p and λ, extracted from Fourier analysis. The standard deviations $d\lambda$ account for the spread of the wavelength, which at very low amplitudes/accelerations is specially high. The range of amplitudes A and accelerations Γ investigated was devised to capture the development of the instability; the width of the system L was chosen to ensure that a sufficient number of wavelengths fit the simulation window – so the errors in the determination of λ are diminished. These results will be discussed in § 5 and compared with the results of the computational hydrodynamics.

Hydrodynamic fields such as density, velocity and temperature were generated from 50 cycles of the MD simulation at amplitude $A = 5.6\,\sigma$ (σ is particle diameter) and frequency $f = 3.5$ Hz, so that they could be compared with the respective fields from the HD simulation. For this purpose we used a $150\,\sigma \times 50\,\sigma$ grid. The positions and velocities of all particles were recorded for 50 periods at a rate of 50 fixed equidistant

phases per period. In order to generate hydrodynamic fields, phase averaging was performed over particle positions and velocities with a spatial coarse graining function (Goldhirsch 1999) $\phi(\boldsymbol{r}) \propto \theta(\sigma/2-|\boldsymbol{r}-\boldsymbol{r}_i(t)|)$ where θ is the Heaviside step function and $\boldsymbol{r}_i(t)$ the instantaneous location of the centre of a particle. The cell size for averaging fits about 3×1 particles, which leaves us with a typically mesoscopic procedure.

4.3. *Set-up for the hydrodynamic system*

We solve the full set of equations in two dimensions (2.7) supplied with the kinetic coefficients given by (2.11)–(2.14) and the equation of state (2.10) on a $150 \times (50 \text{ up to } 100)$ rectangular grid. The initial state is prepared by allowing the material to settle under the action of gravity and form a deposited layer of 6 grains. The depth of the granular bed is imposed by assuming a close random packing density in the deposited layer. As in MD simulations, the diameter of the grains is $\sigma = 10$ mm and their restitution $e = 0.75$.

The domain in which the hydrodynamic equations are solved varies between 300σ and 600σ in the x_1-direction, and between 30σ and 100σ in the vertical or x_2-direction for the range of amplitudes A and frequencies f tested in the simulations (1.5σ to 15σ in amplitude, 2 to 6 Hz in frequency). In this way we make sure that the scale of the pattern is correctly modelled and a sufficient number of pattern wavelengths are captured. The choice of the vibration parameters is adjusted to cover the bifurcation region; that is, the region in which the granular layer destabilizes from the homogeneous (in the x_1-direction) solution. In general, we use exactly the same values for the parameters as in the MD simulations.

Let us again point out that the moving boundary is treated by changing the reference frame to that of the oscillating piston. As a consequence, (2.11)–(2.14) are solved in a fixed rectangular domain with a total force field composed by the gravity and the oscillating harmonic term from the change in the reference frame. The ceiling then oscillates with the moving plate.

We use periodic boundary conditions along the x_1-direction, while at the top and the bottom we set reflecting boundaries. Boundary conditions for the kind of numerical methods introduced in § 3 are set by imposing the values of the computed quantities–density, velocity and total energy–on a buffer of ghost points outside the computational domain. For a WENO5 method, we need three ghost points outside the computational grid. Periodic boundary conditions are approximated by copying all values of the computed quantities from the other end of the periodic boundary to the ghost points. Reflecting boundaries are simulated by using mirror symmetry with respect to the wall to flip all values of the computed quantities from inside the computational domain to the ghost points while changing the sign of the vertical velocity. Reflecting boundaries set in this manner numerically impose conditions of impenetrability and zero total energy flux through the solid walls, i.e. zero normal derivative for the density and the total energy, and $U_2 = 0$ on the top and the bottom walls.

The top wall is set at a distance at which reflections are of minor importance (the packing fraction at these heights is always of the order of 10^{-4}). The hydrodynamic fields (density, velocity components, temperature) are stored for subsequent inspection without any additional treatment. Since the homogeneous solution tends to be very stable in the absence of random sources, we numerically perturb the layer density with a collection of modes (the first 20 of which have the longest wavelengths) at random phases and amplitudes. The latter are selected so that their maximum is of the order of 10^{-3} times the value of the local packing fraction of the deposited
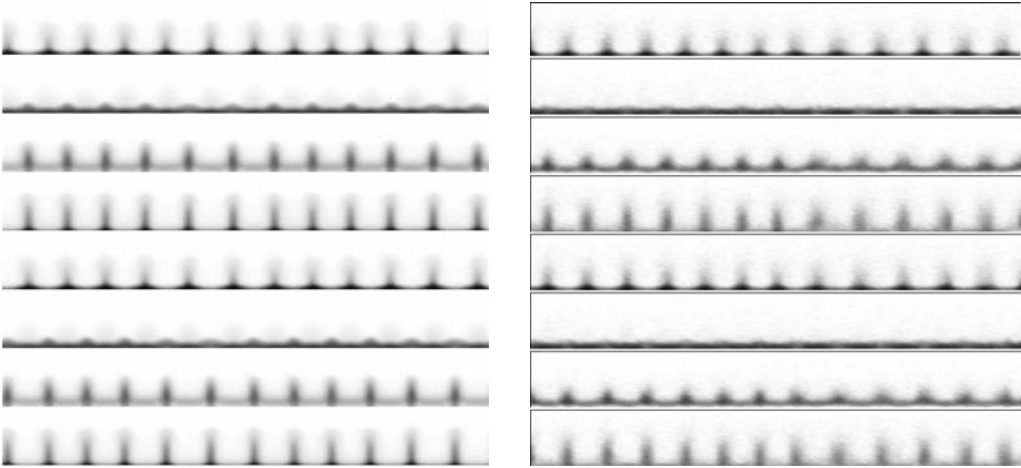
FIGURE 2. Eight pictures of the density as obtained from the numerical solution of the hydrodynamic equations (HD, left) and the corresponding ones from the molecular dynamics simulation (MD, right). The times for the HD snapshots are: 0, $0.25T$, $0.5T$, $0.75T$, T, $1.25T$, $1.5T$, $1.75T$, with T being the oscillation period. The MD snapshots were taken at times: 0, $0.25T$, $0.5T$, $0.86T$, T, $1.25T$, $1.5T$, $1.86T$. The initial phase is arbitrary, but common to both sets. For most of the period, the dynamics observed in HD and MD simulations is completely equivalent; the difference in the third and seventh phases is due to different landing times of the granular bed (see text). The MD figures are obtained after averaging particle positions over 50 cycles, while the density field on the left is the raw output. The frequency of vibration is $f = 3.5$ Hz and the amplitude $A = 5.6$ diameters. Complete sequences are available as movie 3 with the online version of the paper.

material. This small perturbation is sufficient for the growth of the mode selected by the system to be observed which gives rise to the development of the Faraday waves (see movie 2 available with the online version of the paper).

5. Results

Unlike particle simulations, in hydrodynamic simulations the patterns tend to be very stable and regular. The selected wavelength grows within 10 cycles once the perturbation has been imposed, and only minor changes are observed after this time. The periodicity of the pattern is twice the shaking period, as corresponds to the typical period doubling of this instability. Figure 2 shows the appearance of the pattern in a sequence of eight frames which covers two shaking periods and the corresponding frames generated from the MD simulation.

The main difference between the HD and MD sequences in figure 2 is the different landing time of the granular bed. The fourth and the eighth snapshots were taken when the material visibly started to deposit, which happened at different times in HD and MD simulations. This deserves careful discussion. One of the typical features accompanying the instability is the gap formed between the material and the bottom wall, induced by an acceleration of the plate at $\Gamma > 1$. In both real experiments and MD simulations – and ignoring the effects of particle noise – there is a true empty space that periodically opens and closes. In HD simulations, the density is never very close to zero at the bottom wall. This has to be attributed to the implemented boundary condition. More will be said about this later in this section.

The bifurcation diagram (figure 3) clearly shows the extent of the agreement between both types of simulations. The results quantitatively diverge by no more
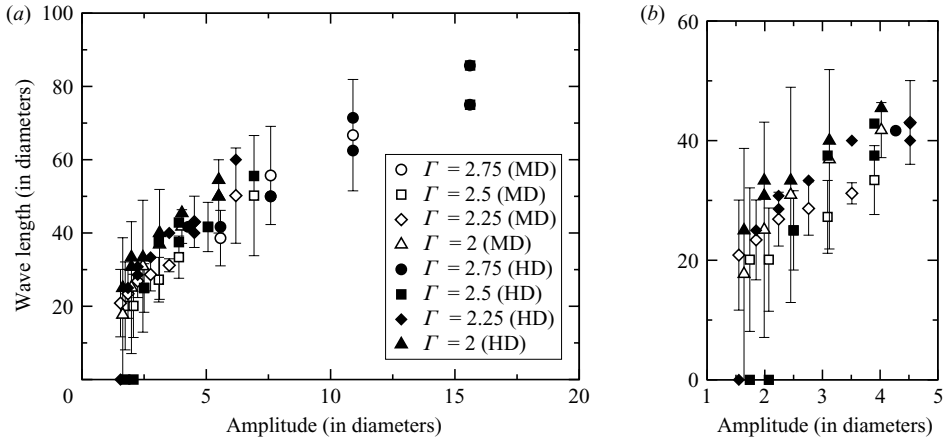
FIGURE 3. The wavelength of the pattern as a function of the amplitude of shaking, for different reduced accelerations Γ. Filled symbols, numerical solution of the hydrodynamic equations; open symbols, event-driven molecular dynamics simulations. (*b*) An enlargement of the figure at low amplitudes. Error bars are drawn only for MD datapoints.

than 20%. Close to the bifurcation point, though, there is an important exception: according to the hydrodynamic simulations, the pattern starts to form between 1.55 and 1.64 diameters of amplitude, since below $A = 1.64\sigma$ it is not observed at any reduced acceleration $\Gamma = A(2\pi f)^2/g$ in the range from 2.0 to 2.75, where g is the acceleration due to gravity. The MD simulations, however, provide a few non-zero wavelengths in the region of very low amplitudes. Nevertheless the errors associated with these MD measures are particularly large, and come from the procedure for determining the characteristic pattern wavelength in MD simulations: owing to the general contribution of particle noise, the wavelength was extracted from the histogram of the Fourier analysis of the particle positions over 50 periods. Otherwise, in the low-amplitude regime, no pattern would be discerned by visual inspection of the MD sequences. Therefore, the typical histograms contain a wide spread of wavelengths in this regime, which is reflected in the standard deviations ($d\lambda$ in table 1) plotted in figure 3 as error bars. The duplicate data points in some of the hydrodynamic samples are situations where a child peak develops or disappears (owing to finite size effects introduced by the periodic boundaries) and, as a result, both wavelengths can be observed in the course of one simulation. This tends to happen in the large-amplitude regime (outside the enlarged region in figure 3), where the pattern is less stable. Patterns in the MD simulation are not so stationary, particularly at low amplitudes. However, the pattern formation phenomenon is quite robust in hydrodynamic simulations.

Figure 4 shows the obtained MD and HD wavelengths as a function of the frequency. The curves represent different theoretical approaches. Luding (1997*b*) showed that the empirical curve (dashed line)

$$\lambda = \sqrt{H}\left(\lambda^* + \frac{g^*}{f^2}\right), \tag{5.1}$$

with the values for the constants $\lambda^* = 7.2$ mm and $g^* = 1.35$ m s^{-2}, obtained in a quasi-two-dimensional experiment with aluminium particles, fitted successfully his MD results. However, we cannot expect that the empirical curve fits the wavelengths
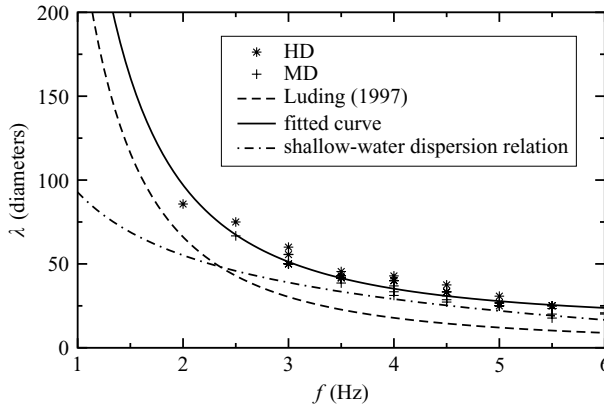
FIGURE 4. Fit of the wavelength as a function of the frequency (solid curve). The dashed and dot-dashed curves are the empirical fit and the shallow-water dispersion relation, respectively (Luding 1997*b*). See text for a detailed explanation.

obtained for our frictionless particles. As a matter of fact, we obtain a different set of constants for the same type of fitting function: $\lambda^* = 6.0$ mm and $g^* = 1.35$ m s^{-2} (solid curve). The dash-dot curve corresponds to the shallow-water dispersion relation $\omega^2/4gk = \tanh(hk)$ (Luding 1997*b*), from which both the present fit and the empirical curve depart at low frequencies.

Figure 5 shows a two-period sequence of the vertical profiles of the packing fraction ν and the rescaled internal energy $\nu T/\sigma g$, as a function of height in diameters. For the plots, we have selected one of the locations in figure 2 where a valley/cusp develops alternately. Figure 5(*a*) shows the granular material that is already being compressed by the incoming bottom wall. As can be seen, the layer (solid line) is small so the profile corresponds to the location of a valley at this time. The thermal energy is high and has started to propagate upwards after the impact. The shock wave can be identified by the quick rise in the thermal energy along with a simultaneous compression of the suspended (cold, dilute) granular layer seen at the bottom of the density profile. In figure 5(*b*) the layer is thickening while at the peaks it is thinning, as figure 5(*f*) shows. In figure 5(*c*), the energy has already propagated to the top, the material is suspended and rather fluidized, and the cusp is visible. In figure 5(*d*), another impact is taking place, the density is growing at the bottom, and one more shock wave has been generated, the energy of which fades as the peak redissolves to feed the closest locations where new cusps are forming. Indeed, in figure 5(*e*), the material is closely packed at the bottom, so density can only further decrease by pressure gradients. The comparison between figures 5(*c*) and 5(*g*) shows that the densities are very different in peaks and valleys, so the shock progresses differently: the energy rises to the highest values at the cusps, whereas at the valleys the energy peak is less pronounced. Let us emphasize that figures 5 and 8 show the rescaled internal energy $\nu T/\sigma g$ instead of the temperature profiles. The reason is the high level of particle noise in the MD results above the granulate. However, we can also interpret the results in terms of temperature. For example, since in figure 5(*c*) the internal energy is broadly constant whilst the packing fraction decays, the granular temperature in fact increases with height, showing the remnants of the shock wave propagation through the cusps.

A careful analysis of the shock wave propagating through a homogeneous vibrated bed (i.e. the stationary flat state) has been done by Bougie *et al.* (2002) and here it
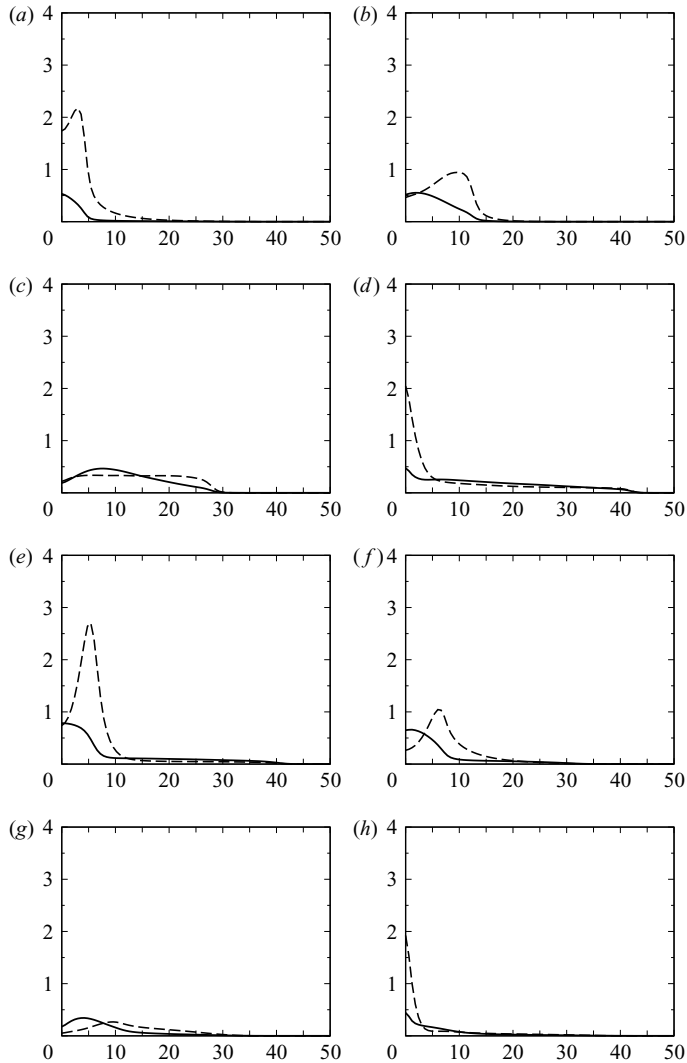
FIGURE 5. Hydrodynamic simulation: a two-period sequence of the vertical profiles of the packing fraction ν (solid line) and the rescaled internal energy $\nu T/\sigma g$ (dashed) as a function of height, in diameters, for the same times as the snapshots in figure 2 (left-hand side).

suffices to point out that the flow is indeed supersonic. The Mach numbers range from 0 to 10 (see figure 6 for the typical oscillations of the Mach number in valleys and cusps). The Mach numbers are highest in the dilute phase, but not far from the dense phase. The figure shows the Mach number that was recorded at the height at which the packing fraction is 5%, which is a convenient measure of the interface between the dense and rarefied material. The convective motion along the x_1-direction, which removes material from the dense towards the dilute locations, will be analysed below.

For the MD simulation, the time-dependent thermal energy was extracted by averaging over 50 cycles the corresponding phases of the local fluctuational kinetic energy, as defined by (2.5). Afterwards an average over equivalent locations was performed. The profiles are shown in figure 8. Comparison between figures 5 and
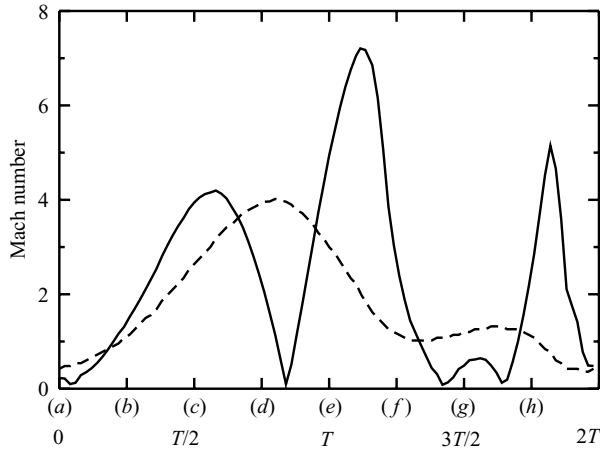
FIGURE 6. Solid line, evolution of the Mach number over two periods for the frames in figure 5 at a height (variable) at which the packing fraction is 5%. Dashed line, height (in diameters divided by 10) corresponding to the values of the Mach number shown.

8 indicates that the quantitative difference in the rescaled internal energy profiles is small. The density profiles show that the maximum packing fraction of the MD averaged field is also very similar to the HD result, about 0.75. This agreement justifies the use of $\nu_c = 0.82$ in our hydrodynamic computations, rather than the hexagonal packing fraction 0.92 as the critical density, as said previously. However, the hydrodynamic profiles show a sharper shock wave than their corresponding MD counterparts. This is related to the residual heating observed in MD simulations at heights at which the granular layer is sufficiently dilute (very visible for example in figure 8*f*). A movie of the complete sequences is available with the online version of the paper (movie 4). The maximum values of the temperature do not differ significantly, whereas the MD profiles appear to be systematically thicker. This phenomenon might be partly due to the mesoscopic averaging procedure used here. It is known, on the other hand, that hydrodynamic variables can be scale dependent in granular systems (Goldhirsch 2001) owing to the lack of scale separation. So even if the number of samples (cycles) could in principle be increased, and therefore the mean fields better defined, the local noise would persist at scales of the order of one particle (which is the grid size used here for averaging the MD sequences), particularly in dilute regions. The number of samples is practically limited by the fact that the MD pattern is not strictly stationary for very long. It is not desirable either to increase the grid size for averaging, for obvious reasons: here, where the pattern is of the size of a few grains, the fields obtained from MD simulations would lose structure and definition. On the other hand, the granular Navier–Stokes equations (2.7) do not account for such a source of fluctuations. The effect of varying the grid size on the hydrodynamic fields extracted from MD simulations is shown in figure 7. There we plot the maximum of the packing fraction and the rescaled thermal energy obtained from the sequence of profiles, as a function of the vertical grid size for averaging (the horizontal grid size is kept constant). In the vertical direction, the profiles are expected to be sharper, so a loss of information could occur due to an inadequate averaging procedure. The sequences analysed consist of 100 frames over two oscillation periods, and the granular motion is sufficiently time resolved for our purposes. An average over locations occupied by cusps/valleys has been also applied along the entire system.
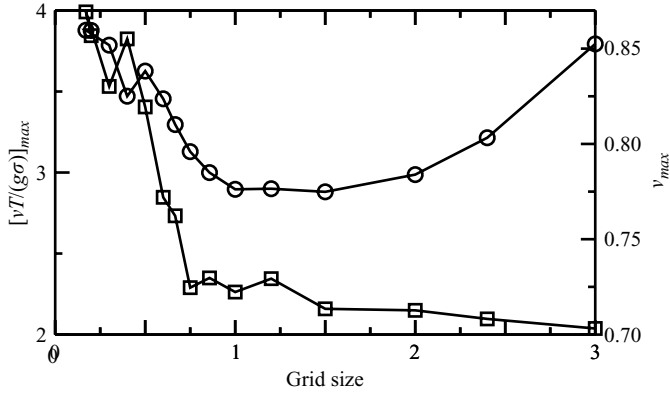
FIGURE 7. The maximum packing fraction (squares) and rescaled thermal energy (circles) obtained from averaging the MD sequences for different vertical grid sizes (the horizontal grid size is kept constant).

Figure 7 shows several regions. At grid sizes of the order of one particle diameter, the averages produce stable results. For sizes below one particle diameter, the maximum values for the density and thermal energy vary quickly. In this latter range of grid sizes, we would require a larger number of periods in order to extract reliable results for the mean fields. For grid sizes larger than one, the maximum packing fraction decreases and the thermal energy increases. Thus, grid sizes of about one particle diameter are shown to render the most reasonable results. As a conclusion: under the limitations discussed, good quantitative agreement can be achieved with mesoscopic statistics: a manageable number of samples (25) and a one-diameter characteristic cell size, along with a final average of means over corresponding locations.

There is still another difference between the MD and HD profiles: the gap formed when the granular layer takes off (figure 2c, g). In MD simulations, when the wall moves downward, the entire layer levitates, as we can see in the corresponding frames in figure 8 by noting that the density at zero height is exactly zero. However, in HD simulations, the density at the bottom is never very close to zero. It is particularly large at the base of the cusps, (figure 5c), where the packing fraction is 0.19. Seemingly, the hydrodynamic layer is stickier, or behaves more inelastically, than the MD granular bed. In addition, in hydrodynamic simulations, the fact that there is some material stuck to the bottom during take off anticipates the impact with the wall and the corresponding generation of the shock wave. This is the source of the mismatch between the landing times, to which figure 2 refers. The shock is anticipated in HD simulations because there is no empty space between the granular material and the plate. Instead, in MD simulations, the plate travels through the gap without encountering any material to collide with. The anticipation of the shock wave in the HD simulation can be clearly seen when the online movies for the thermal energy are compared: the maximum of the energy peak occurs a few frames before (exactly 1/10 of the oscillating period) in the HD sequence. Afterwards the MD sequence catches up until the next impact with the plate. As said above, the absence of gap in the HD simulation is probably due to the inadequacy of the boundary conditions used (impenetrable, adiabatic plate). It is worth mentioning that Bougie *et al.* (2002) see a substantial gap when solving the HD equations for a homogeneous granular bed in three dimensions and with a larger restitution coefficient $e = 0.9$ and larger amplitude $\Gamma = 3$. This larger gap is due to the different choice of parameters and it
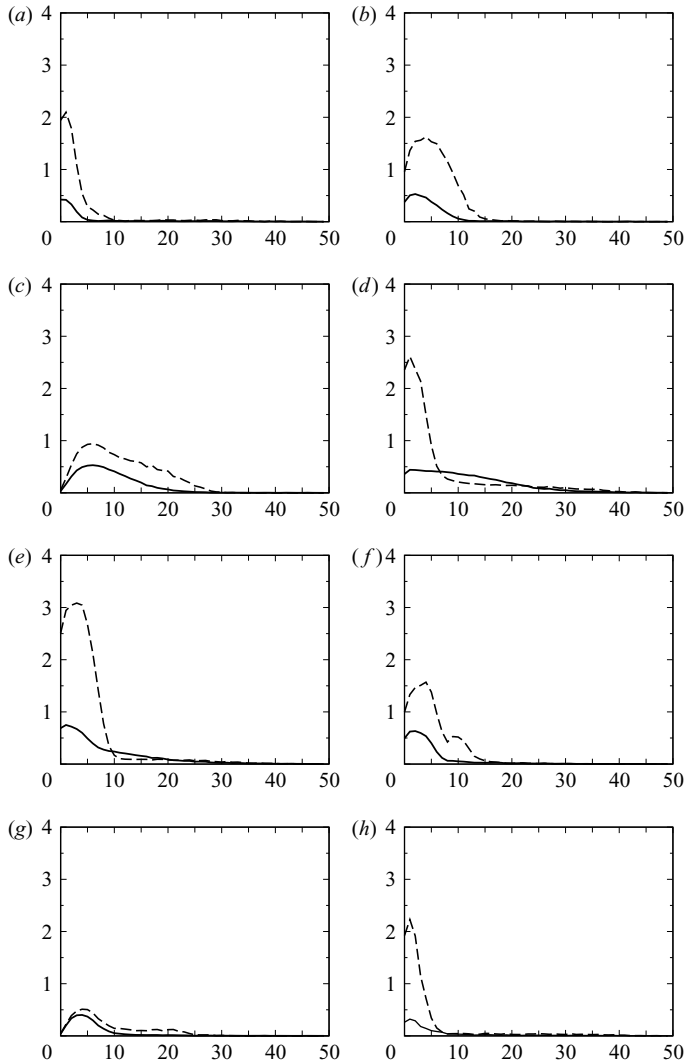
FIGURE 8. Molecular dynamics simulation: a two-period sequence of the vertical profiles of the packing fraction ν (solid line) and the rescaled internal energy $\nu T/\sigma g$ (dashed) as a function of height, in diameters, for the same times as the snapshots in figure 2 (right-hand side).

does not change the main conclusion on the drawbacks of the boundary conditions for the HD simulation. Our simulations too, render a bigger gap size and smaller packing fraction at the bottom plate ($\simeq 0.04$) for flat states at $\Gamma = 3$ and for $e = 0.9$. However, when the restitution coefficient is lowered to $e = 0.75$, keeping the rest of the parameters constant, the gap is reduced and the minimal packing fraction at the bottom increases again up to $\simeq 0.20$.

It is worth analysing the velocity field and the convection pattern which accompanies the Faraday waves. These are shown in values that are relative to the velocity of the plate in figures 9 and 10 for hydrodynamic and MD simulations, respectively, and in movie 5 available with the online version of the paper. In fact what is shown is the linear momentum field rather than the velocity, in order to focus on the most important part of the system and remove from the picture the almost
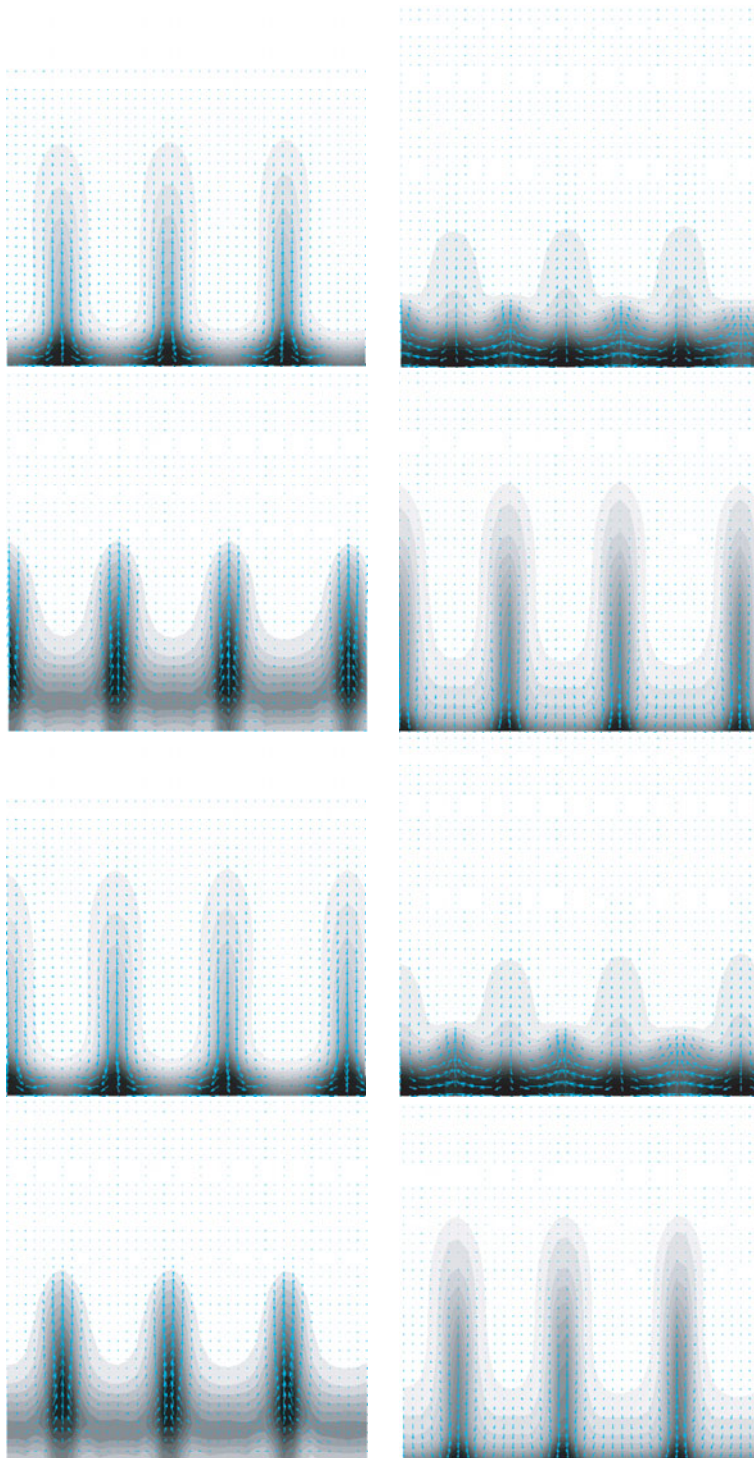
FIGURE 9. Hydrodynamic simulation: the linear momentum plotted over the density field in grey shades. The frames are taken at the same times as in figure 2 (left-hand side) and cover two cycles of the driving oscillation. A movie is available with the online version of the paper (movie 5).
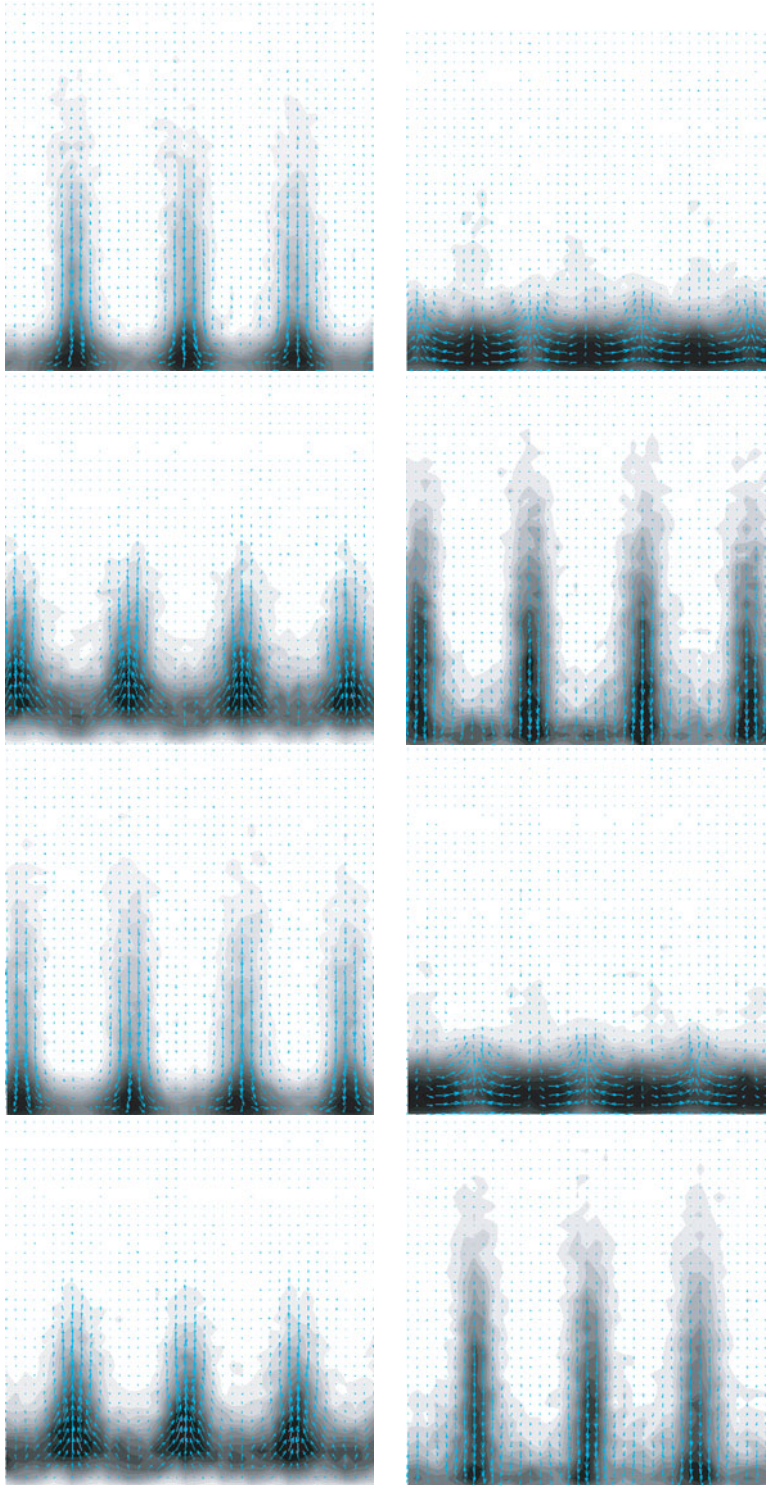
FIGURE 10. Molecular dynamics simulation: the linear momentum plotted over the density field in grey shades. The frames are taken at the same times as in figure 2 (right-hand side) and cover two cycles of the driving oscillation.

empty regions, in which the MD averages are too noisy. Comparing both panels we again see the effect that was pointed out above: in hydrodynamic simulations, the material is always in contact with the vibrating plate. This has been observed before in hydrodynamic simulations of vibrated granular layers without pattern formation (M. Shattuck personal communication). In figures 9 and 10 we observe that material is removed from the dense regions and taken towards the loose regions after each impact on the wall, during the alternate formation of cusps. The scaling factor for the arrows is identical for both figures and again reveals good quantitative agreement of HD and MD simulations. In HD, the linear momentum values are about 20% lower than in the MD simulations: the maximum value for the linear momentum was 1.17 in I.S. units for the MD sequence and 0.935 for the HD simulation. Note that simple reflecting boundaries are used at the plate for the hydrodynamic simulations, and that particles are perfectly smooth in MD simulations. It is difficult to evaluate the effect of the choice of boundary conditions on the dynamics in more complex set-ups, but in view of the results, it seems clear that this undisturbed sliding along the plate looks like the only reasonable choice in this very simple situation.

6. Conclusions

So far we have compared the results given by the two simulation methods considered: the traditional approach by event-driven MD and the hydrodynamic approach by means of a CFD code.

6.1. *Numerical aspects*

It is worth comparing the efficiency of the two methods in general. In the first place, CFD codes are computationally expensive. On the other hand, the scale of the gradients is one particle diameter: effectively, the cell size cannot be greater than a few particles. At Mach numbers of about 10 in some phases of the motion, inertia is the most prominent mechanism of transport. Diffusion operates at very small length scales, and is of less importance than inertia, but plays a role in other phases of the motion, when the typical Mach number drops below 1 in the dense phase, and cannot just be neglected. In addition, explicit time schemes like the one used in this paper introduce a stability condition which becomes more restrictive as the diffusion length scales (the size of the particles) become smaller. The result is that for submillimetric particles, most commonly used in real experiments, the same problem treated here becomes very stiff and thus, we should resort to an implicit treatment of the viscous and/or cooling terms.

In any case, length scales that are typically one particle in size must be resolved, and the ratio one cell $\approx$ one particle is extremely unfavourable to computational hydrodynamics in terms of efficiency. Moreover, high-resolution shock-capturing schemes like WENO add an extra cost to the computation which often takes the largest amount of the total CPU time. There is some room for optimization though. Such extraordinary effort need not be made to construct highly accurate numerical fluxes everywhere and all the time, so simulation time could be reduced in this way.

6.2. *Physical aspects*

We have shown that both qualitatively and quantitatively, finely tuned state-of-the-art hydrodynamic codes can reproduce the features of particle simulations in complex flow problems dealing with transient strong shock waves and pattern formation, such as the Faraday instability investigated here. In particular, the appearance and wavelength of the pattern have been reproduced with a very good approximation

as seen from the bifurcation diagram (figure 3). The hydrodynamic fields compare very well to the corresponding averaged particle fields. However, further investigation should be carried out to improve the boundary conditions so that the gap between the plate and the granulate during cusps is larger. The hydrodynamic temperature is shown to agree with its MD counterpart to which ensemble averaging at a typical grid size of one particle diameter has been applied. Finally, the velocity field obtained in hydrodynamic simulations follows the same structure as the particle velocity field, even though it gives somewhat smaller values. The discrepancies found throughout the analysis are of the order of 20%.

Finally, we should ask why the agreement between molecular dynamics and hydrodynamics is so good here, so robust, when everything suggests that it should not be. At high densities collisions are not binary, fluxes are thus non-local and the expressions for the kinetic coefficients should no longer apply, not to mention the degree of inelasticity (the restitution is only $e = 0.75$) which invalidates the assumption of small gradients on which all kinetic theory expansions are based. It seems that there is only one reason for the agreement: the dynamics is mostly Eulerian and such details as constitutive relations and transport coefficients are not definitive. So much so that, in practice, if the shock wave is modelled accurately and a suitable equation of state is introduced, the instability can be 'easily' reproduced, as in molecular dynamics, with the essential contribution of inelasticity. Unfortunately, we cannot simulate Eulerian granular flow with the present implementation of the code without the diffusive terms in the Navier–Stokes equations. If we neglect them completely, the stability of the code is compromised.

We found several hints in support of this statement. The first one is the evolution of the Mach number (figure 6), showing that the flow is supersonic during large portions of the two-cycle periodic motion. The second is the result (not presented here) obtained from two types of simulation which approach the Euler limit: (i) by multiplying all kinetic coefficients by a factor of 0.2; and (ii) by switching off selectively all diffusion terms but one. In both tests, we obtained the same wavelengths as in the case of the full Navier–Stokes equations.

Appendix. Formulae for local variables

Here, we summarize the formulae for the explicit eigenvalues and eigenvectors of the Jacobian matrix of the Euler part of (3.1) in two dimensions, for general equations of state depending on the density and the enthalpy. As discussed in § 3, the system (3.1) can be rewritten as

$$\frac{\partial \boldsymbol{u}}{\partial t} + \frac{\partial}{\partial x_1} \boldsymbol{f}(\boldsymbol{u}) + \frac{\partial}{\partial x_2} \boldsymbol{g}(\boldsymbol{u}) = \boldsymbol{S}(\boldsymbol{u}), \tag{A1}$$

with obvious definitions for $\boldsymbol{f}(\boldsymbol{u})$, $\boldsymbol{g}(\boldsymbol{u})$ and $\boldsymbol{S}(\boldsymbol{u})$ and with the vector $\boldsymbol{u} = (u_1, u_2, u_3, u_4)$ whose components are given by

$$\left.\begin{array}{l} u_1 = \rho, \quad u_2 = \rho U_1, \quad u_3 = \rho U_2 \\ u_4 = \rho\epsilon + \tfrac{1}{2}\rho\,|\boldsymbol{U}|^2 = \rho\epsilon + \tfrac{1}{2}\rho\left(U_1^2 + U_2^2\right). \end{array}\right\} \tag{A2}$$

The components of f are

$$f_1(u) = u_2, \qquad f_2(u) = p + \frac{u_2^2}{u_1},$$
$$f_3(u) = \frac{u_2 u_3}{u_1}, \qquad f_4(u) = \frac{u_2}{u_1}(p + u_4), \qquad (A3)$$

where the pressure is assumed to be a function of density and enthalpy,

$$p = p(\rho, \epsilon) = p\left(u_1, \frac{u_3}{u_1} - \frac{1}{2}\frac{u_2^2}{u_1^2}\right). \qquad (A4)$$

Remember that the sound speed is given by (3.5). Given the auxiliary function $H = (p + u_4)/u_1$, the eigenvalues of the Jacobian matrix $f'(u)$ are given by

$$\Lambda_- = \frac{u_2}{u_1} - c_s, \qquad \Lambda_2 = \Lambda_3 = \frac{u_2}{u_1}, \qquad \Lambda_+ = \frac{u_2}{u_1} + c_s, \qquad (A5)$$

and their corresponding right and left eigenvectors are

$$r_\pm = \begin{pmatrix} 1 \\ u_2/u_1 \pm c_s \\ u_3/u_1 \\ H \pm (u_2/u_1)c_s \end{pmatrix}, \qquad r_2 = \begin{pmatrix} 1 \\ u_2/u_1 \\ u_3/u_1 \\ H - 1/b_1 \end{pmatrix}, \qquad r_3 = \begin{pmatrix} 0 \\ 0 \\ 1 \\ u_3/u_1 \end{pmatrix}, \qquad (A6)$$

and

$$l_\pm = \begin{pmatrix} \frac{1}{2} \mp \frac{u_2}{u_1}\frac{1}{2c_s} + \frac{b_1}{2}\left(\frac{u_2^2 + u_3^2}{u_1^2} - H\right) \\ -\frac{b_1}{2}\frac{u_2}{u_1} \pm \frac{1}{2c_s} \\ -\frac{b_1}{2}\frac{u_3}{u_1} \\ \frac{b_1}{2} \end{pmatrix}, \qquad l_2 = \begin{pmatrix} \left[H - \frac{u_2^2}{u_1^2} - \frac{u_3^2}{u_1^2}\right]b_1 \\ \frac{u_2}{u_1}b_1 \\ \frac{u_3}{u_1}b_1 \\ -b_1 \end{pmatrix}, \qquad l_3 = \begin{pmatrix} -\frac{u_3}{u_1} \\ 0 \\ 1 \\ 0 \end{pmatrix}, \qquad (A7)$$

respectively, where $b_1 = p_\epsilon/\rho c_s^2$. For the fluxes associated with the x_2-derivative, that is,

$$g_1(u) = u_3, \qquad g_2(u) = \frac{u_2 u_3}{u_1}, \qquad (A8a, b)$$

$$g_3(u) = p + \frac{u_3^2}{u_1}, \qquad g_4(u) = \frac{u_3}{u_1}(p + u_4); \qquad (A8c, d)$$

we only need swap indices 2 and 3 in all formulae above, and the second and third components in all right and left eigenvectors.

REFERENCES

AOKI, K. M. & AKIYAMA, T. 1996 Spontaneous wave pattern formation in vibrated granular materials. *Phys. Rev. Lett.* **77**, 4166–4169.

AOKI, K. M. & AKIYAMA, T. 1997 Reply on Bizon *et al.* (1997). *Phys. Rev. Lett.* **79**, 4714.

BIZON, C., SHATTUCK, M. D., NEWMAN, J. T., UMBANHOWAR, P. B., SWIFT, J. B., McCORMICK, W. D. & SWINNEY, H. L. 1997 Comment on Aoki & Akiyama (1996). *Phys. Rev. Lett.* **79**, 4713.

BIZON, C., SHATTUCK, M. D. & SWIFT, J. B. 1999 Linear stability analysis of a vertically oscillated granular layer. *Phys. Rev.* E **60**, 7210.

BOBYLEV, A. V., CARRILLO, J. A. & GAMBA, I. M. 2000 On some properties of kinetic and hydrodynamic equations for inelastic interactions. *J. Stat. Phys.* **98**, 743–773.

BOUGIE, J., MOON, S. J., SWIFT, J. & SWINNEY, H. 2002 Shocks in vertically oscillated granular layers. *Phys. Rev.* E **66**, 051301.

BOUGIE, J., KREFT, J., SWIFT, J. B. & SWINNEY, H. 2005 Onset of patterns in an oscillated granular layer: continuum and molecular dynamics simulations. *Phys. Rev.* E **71**, 021301.

BRILLIANTOV, N. V. & PÖSCHEL, T. 2004 *Kinetic Theory of Granular Gases*. Oxford University Press.

BRILLIANTOV, N. V., SPAHN, F., HERTZSCH, J.-M. & PÖSCHEL, T. 1996 A model for collisions in granular gases. *Phys. Rev.* E **53**, 5382.

BRILLIANTOV, N. V., SALUEÑA, C., SCHWAGER, T. & PÖSCHEL, T. 2004 Transient structures in a granular gas. *Phys. Rev. Lett.* **93**, 134301.

CLÉMENT, E., VANEL, L., RAJCHENBACH, J. & DURAN, J. 1996 Pattern formation in a vibrated 2D granular layer. *Phys. Rev.* E **53**, 2972–2975.

VAN DOORN, E. & BEHRINGER, R. P. 1997 Onset and evolution of a wavy instability in shaken sand. *Phys. Lett.* A **235**, 469.

DOUADY, S., FAUVE, S. & LAROCHE, C. 1989 Subharmonic instabilities and defects in a granular layer under vertical vibrations. *Europhys. Lett.* **8**, 621–627.

FARADAY, M. 1831 On a peculiar class of acoustical figure and on certain forms assumed by groups of particles upon vibrating elastic surfaces. *Phil. Trans. R. Soc. Lond.* **121**, 299.

GARZÓ, V. & DUFTY, J. W. 1999 Dense fluid transport for inelastic hard spheres. *Phys. Rev.* E **59**, 5895–5911.

GOLDHIRSCH, I. 1999 Scales and kinetics of granular flows. *Chaos* **9**, 659–672.

GOLDHIRSCH, I. 2001 Probing the boundaries of hydrodynamics. In *Granular Gases* (ed. T. Pöschel & S. Luding), Lecture Notes in Physics, vol. 564, pp. 79–99. Springer.

GOLDHIRSCH, I. 2003 Rapid granular flows. *Annu. Rev. Fluid Mech.* **35**, 267.

GOLDSHTEIN, A. & SHAPIRO, M. 1995 Mechanics of collisional motion of granular materials. Part 1. General hydrodynamic equations. *J. Fluid Mech.* **282**, 75–114.

HILL, S. A. & MAZENKO, G. F. 2003 Granular clustering in a hydrodynamic simulation. *Phys. Rev.* E **67**, 061302.

JENKINS, J. & RICHMAN, M. W. 1985a Grad's 13-moment system for a dense gas of inelastic spheres. *Arch. Rat. Mech. Anal.* **87**, 355.

JENKINS, J. & RICHMAN, M. W. 1985b Kinetic theory for plane flows of a dense gas of identical, rough, inelastic, circular disks. *Phys. Fluids* **28**, 3485.

JIANG, G. & SHU, C.-W. 1996 Efficient implementation of weighted eno schemes. *J. Comput. Phys.* **126**, 202.

KAMENETSKY, V., GOLDSHTEIN, A., SHAPIRO, M. & DEGANI, D. 2000 Evolution of a shock wave in a granular gas. *Phys. Fluids* **12** (11), 3036–3049.

LUDING, S. 1997a Surface waves and pattern formation in vibrated granular media. In *Powders and Grains '97* (ed. R. P. Behringer & J. T. Jenkins), p. 373. Balkema.

LUDING, S. 1997b *Die Physik kohäsionsloser granularer Medien*. Habilitation thesis, Institut für Computeranwendungen 1 (Stuttgart).

LUDING, S. & MCNAMARA, S. 1998 How to handle the inelastic collapse of a dissipative hard-sphere gas with the TC model. *Granular Matter* **1**, 113–128.

LUDING, S., CLÉMENT, E., RAJCHENBACH, J. & DURAN, J. 1996 Simulations of pattern formation in vibrated granular media. *Europhys. Lett.* **36**, 247–252.

LUTSKO, J. F. 2005 Transport properties of dense dissipative hard-sphere fluids for arbitrary energy loss models. *Phys. Rev.* E **72**, 021306.

MCNAMARA, S. & YOUNG, W. R. 1993 Inelastic collapse in two dimensions. *Phys. Rev.* E **50**, R28–R31.

MEERSON, B., PÖSCHEL, T. & BROMBERG, Y. 2003 Close-packed floating clusters: granular hydrodynamics beyond the freezing point? *Phys. Rev. Lett.* **91**, 24301.

MEERSON, B., PÖSCHEL, T., SASOROV, P. V. & SCHWAGER, T. 2004 Giant fluctuations at a granular phase separation threshold. *Phys. Rev.* E **69**, 21302.

MELO, F., UMBANHOWAR, P. & SWINNEY, H. L. 1994 Transition to parametric wave patterns in a vertically oscillated granular layer. *Phys. Rev. Lett.* **72**, 172–175.

MELO, F., UMBANHOWAR, P. & SWINNEY, H. L. 1995 Hexagons, kinks, and disorder in oscillated granular layers. *Phys. Rev. Lett.* **75**, 3838–3841.

METCALFE, T., KNIGHT, J. B. & JAEGER, H. M. 1997 Surface patterns in shallow beds of vibrated granular material. *Physica* A **236**, 202–210.

MOON, S. J., SWIFT, J. & SWINNEY, H. 2004 Role of friction in pattern formation in oscillated granular layers. *Phys. Rev.* E **69**, 031301.

PAK, H. K. & BEHRINGER, R. P. 1993 Surface waves in vertically vibrated granular materials. *Phys. Rev. Lett.* **71**, 1832.

PARESCHI, L. & RUSSO, G. 2005 Implicit–explicit Runge–Kutta methods and applications to hyperbolic systems with relaxation. *J. Sci. Comput.* **25**, 129.

PÖSCHEL, T. & SCHWAGER, T. 2005 *Computational Granular Dynamics*. Springer.

PÖSCHEL, T., SCHWAGER, T. & SALUEÑA, C. 2000 Onset of fluidization in vertically shaken granular material. *Phys. Rev.* E **62**, 1361.

RAMÍREZ, R., PÖSCHEL, T., BRILLIANTOV, N. V. & SCHWAGER, T. 1999 Coefficient of restitution of colliding viscoelastic spheres. *Phys. Rev.* E **60**, 4465–4472.

RENARD, S., SCHWAGER, T., PÖSCHEL, T. & SALUEÑA, C. 2001 Vertically shaken column of spheres. Onset of fluidization. *Eur. Phys. J.* E **4**, 233.

RERICHA, E., BIZON, C., SHATTUCK, M. & SWINNEY, H. 2002 Shocks in supersonic sand. *Phys. Rev. Lett.* **88**, 1.

ROTHMAN, D. H. 1998 Oscillons, spiral waves, and stripes in a model of vibrated sand. *Phys. Rev.* E **57**, R1239–R1242.

SCHWAGER, T. & PÖSCHEL, T. 1998 Coefficient of restitution of viscous particles and cooling rate of granular gases. *Phys. Rev.* E **57**, 650–654.

SERERO, D., GOLDENBERG, C., NOSKOWICZ, S. H. & GOLDHIRSCH, I. 2007 The classical granular temperature and slightly beyond. Preprint: arXiv:cond-mat/0702545v1.

SHU, C.-W. 1998 Essentially non-oscillatory and weighted essentially non-oscillatory schemes for hyperbolic conservation laws. In *Advanced Numerical Approximation of Nonlinear Hyperbolic Equations* (ed. A. Quarteroni), Lecture Notes in Mathematics, vol. 1697, p. 325. Springer.

SHU, C.-W. & OSHER, S. 1998 Efficient implementation of essentially non-oscillatory shock capturing schemes. *J. Comput. Phys.* **77**, 439.

TORQUATO, S. 1995 Nearest-neighbor statistics for packings of hard spheres and disks. *Phys. Rev.* E **51**, 3170.

TSIMRING, L. S. & ARANSON, I. S. 1997 Localized and cellular patterns in a vibrated granular layer. *Phys. Rev. Lett.* **79**, 213–216.

UMBANHOWAR, P. B., MELO, F. & SWINNEY, H. L. 1996 Localized excitations in a vertically vibrated granular layer. *Nature* **382**, 793–796.

UMBANHOWAR, P. B., MELO, F. & SWINNEY, H. L. 1998 Periodic, aperiodic, and transient patterns in vibrated granular layers. *Physica* A **249**, 1–9.

WASSGREN, C. R., BRENNEN, C. E. & HUNT, M. L. 1996 Vertical vibration of a deep bed of granular material in a container. *J. Appl. Mech.* **63**, 712–719.